

Coseismic and Early Postseismic Deformation of the 2020 Mw6.4 Nima Earthquake, Central Tibet, from InSAR and GNSS Observations

Xiaoli Liu^{1*}, Tao Xia¹, Jing Liu-Zeng^{2*}, Debeier Deng¹, Zhige Jia¹, Peng Wang³, Pengfei Yu¹, Wenqing Wang⁴

¹Institute of Seismology, China Earthquake Administration, China, ²School of Earth System Science, Tianjin University, China, ³Institute of Geology, China Earthquake Administration, China, ⁴The Second Monitoring and Application Center, China Earthquake Administration, China

Submitted to Journal:
Frontiers in Earth Science

Specialty Section:
Structural Geology and Tectonics

Article type:
Original Research Article

Manuscript ID:
1012773

Received on:
05 Aug 2022

Journal website link:
www.frontiersin.org

Conflict of interest statement

The authors declare that the research was conducted in the absence of any commercial or financial relationships that could be construed as a potential conflict of interest

Author contribution statement

X.L. and J.L.-Z. conceived and designed the experiments; X.L., T.X., and D.D. performed the experiments; T.X. and P.Y. analyzed the InSAR data; Z.J., P.W., and W.W. analyzed the GNSS data; X.L. wrote the paper, and all co-authors contributed to the writing. All authors have read and agreed to the published version of the manuscript.

Keywords

tibetan plateau, Normal faulting earthquake, 2020 Nima earthquake, InSAR, GNSS, Coseismic deformation, Postseismic deformation

Abstract

Word count: 328

The 2020 Mw 6.4 Nima earthquake is one of the largest normal-faulting earthquakes recently occurred north of the Banggong suture zone in remote southern Tibet, where geologic investigation of active faults is extremely limited. By investing jointly InSAR and GNSS observations, we calculate the coseismic and initial nine-month postseismic deformation. The optimal model of source geometry suggests this event is the result of moderate-angle east-dipping normal slip on a complex reversed “S-shape” composite structure at fault junctions of the West Yibu-Chaka fault, the Heishi fault, and an unmapped blind fault. Interaction of multiple intersection faults accounted for the larger non-DC component in the long-period point-source solutions. The afterslip released 1.0×10^{18} N·m, about 15.6% of that released by the mainshock and initial eight-day aftershocks. The concentrated stress in the region, especially at the shallow depth of <10 km was released mainly by the mainshock and aftershocks. The >1 bar of postseismic stress increasing in up-dip of the coseismic slip zone indicates the shallow crust of ~4 km between the northern segment of the West Yibu-Chaka fault and the adjacent blind fault crept due to stress perturbations. The >1 bar of postseismic stress increasing along the East Yibu-Chaka fault in downdip of the seismogenic fault implies the deformation source and afterslip extended within the brittle-ductile transition zone. The more than 1 bar of postseismic Coulomb stress increasing around the East Yibu-Chaka fault and the northern of the West Yibu-Chaka fault highlights seismic hazards in the region, especially in the transition zones joined with tail ends of the Riganpei Co and Jiangai Zangbu faults. It is necessary to forecast accurately by longer-term afterslip observation over timescales of years for the faults. Compared with previous studies, our results suggest a more complex subsurface geometry linking the normal and strike-slip faults and more dynamic fault interactions in this poorly-known region of Tibet. Significant postseismic deformation >16 km depth has implications for the rheology of downdip extension of the dipping faults in southern Tibet.

Contribution to the field

The 2020 Mw 6.4 Nima earthquake is one of the largest normal-faulting earthquakes recently occurred north of the Banggong suture zone in remote southern Tibet, where geologic investigation of active faults is extremely limited. We invert jointly the coseismic and postseismic deformation sequence of the 2020 Nima earthquake using InSAR and GNSS displacement datasets within the first nine months after the mainshock. Our results suggest the Nima earthquake ruptured a complex reversed “S-shape” composite structure at fault junctions, which may account for the larger non-DC component in the long-period point-source solutions. The more than 1 bar of postseismic Coulomb stress change around the East Yibu-Chaka fault and the northern of the West Yibu-Chaka fault highlights seismic hazards in the region, especially in the transition zones joined with tail ends of the Riganpei Co and Jiangai Zangbu faults. Compared with previous studies, our results suggest a more complex subsurface geometry linking the normal and strike-slip faults and more dynamic fault interactions in this poorly-known region of Tibet.

Funding statement

Science for Earthquake Resilience, China Earthquake Administration (XH221705C), This work is supported by the National Natural Science Foundation of China (U1839203, 42011540385).

Ethics statements

Studies involving animal subjects

Generated Statement: No animal studies are presented in this manuscript.

Studies involving human subjects

Generated Statement: No human studies are presented in this manuscript.

Inclusion of identifiable human data

Generated Statement: No potentially identifiable human images or data is presented in this study.

In review

Data availability statement

Generated Statement: The original contributions presented in the study are included in the article/supplementary material, further inquiries can be directed to the corresponding author/s.

In review

Coseismic and Early Postseismic Deformation of the 2020 Mw6.4 Nima Earthquake, Central Tibet, from InSAR and GNSS Observations

Xiaoli Liu¹, Tao Xia¹, Jing Liu-Zeng², Debeier Deng¹, Zhige Jia¹, Peng Wang³, Pengfei Yu¹, Wenqing Wang⁴

¹ Institute of Seismology, China Earthquake Administration, Wuhan 430071, China

² School of Earth System Science, Tianjin University, Tianjin 300072, China

³ Institute of Geology, China Earthquake Administration, Beijing 100029, China The second

⁴ Monitoring and Application Center of China Earthquake Administration, Xian 710054, China

* Correspondence:

Xiaoli Liu

liuxl.j@163.com(X. L.)

Jing Liu-Zeng

liu_zeng@tju.edu.cn(J.L-Z.)

Keywords: Tibetan plateau, Normal faulting earthquake, 2020 Nima earthquake, InSAR, GNSS, Coseismic deformation, Postseismic deformation

Abstract

The 2020 Mw 6.4 Nima earthquake is one of the largest normal-faulting earthquakes recently occurred north of the Banggong suture zone in remote southern Tibet, where geologic investigation of active faults is extremely limited. By investing jointly InSAR and GNSS observations, we calculate the coseismic and initial nine-month postseismic deformation. The optimal model of source geometry suggests this event is the result of moderate-angle east-dipping normal slip on a complex reversed “S-shape” composite structure at fault junctions of the West Yibu-Chaka fault, the Heishi fault, and an unmapped blind fault. Interaction of multiple intersection faults accounted for the larger non-DC component in the long-period point-source solutions. The afterslip released 1.0×10^{18} N·m, about 15.6% of that released by the mainshock and initial eight-day aftershocks. The concentrated stress in the region, especially at the shallow depth of <10 km was released mainly by the mainshock and aftershocks. The >1 bar of postseismic stress increasing in up-dip of the coseismic slip zone indicates the shallow crust of ~4 km between the northern segment of the West Yibu-Chaka fault and the adjacent blind fault crept due to stress perturbations. The >1 bar of postseismic stress increasing along the East Yibu-Chaka fault in downdip of the seismogenic fault implies the deformation source and afterslip extended within the brittle-ductile transition zone. The more than 1 bar of postseismic Coulomb stress increasing around the East Yibu-Chaka fault and the northern of the West Yibu-Chaka fault highlights seismic hazards in the region, especially in the transition zones joined with tail ends of the Riganpei Co and Jiangai Zangbu faults. It is necessary to forecast accurately by longer-term afterslip observation over timescales of years for the faults. Compared with previous studies, our results suggest a more complex subsurface geometry linking the normal and strike-slip faults and more dynamic fault interactions in this poorly-known region of Tibet. Significant postseismic

deformation >16 km depth has implications for the rheology of downdip extension of the dipping faults in southern Tibet.

1 Introduction

The Tibetan plateau comprises complex systems of connected and interacting faults. Several NS-trending rift systems developed in the central and southern part of the Tibet Plateau are aligned regularly and nearly perpendicular to the Himalayan collision arc due to the long-term effects of collision and compression of the India-Eurasia plate (Armijo et al., 1989; Tapponnier et al., 2001; Taylor et al., 2003; Kapp et al., 2008; Elliott et al., 2010; Yin and Taylor, 2011) (Figure 1). These rift systems are large in scale and accompanied by multiple groups of NS-trending normal fault systems. They are often associated with large EW-trending strike-slip faults, and together accommodate some of the spatially-varying strains in response to the India-Eurasia plate collision (Wang et al., 2014), and are bounded by the Bangong-Nujiang suture zone (BNS). There are significant differences in E-W extension rate and deformation style on both north and south sides. South of the BNS, the majority of E-W directed extension deformation is accommodated by several N-S normal-faulting systems (Molnar and Tapponnier, 1978; Armijo et al., 1989; Ha et al., 2019; Chevalier et al., 2020), with slip rates in the range of 1~3 mm/a (Harrison et al., 1995; Wu et al., 2015; Ha et al., 2019; Chevalier et al., 2020; Wang et al., 2020). However, the extension is not obvious in the central plateau north of the BNS, and the active tectonics is primarily marked by a series of discrete conjugate strike-slip faults. At the tail end of these faults, N-S normal-faulting plays a subsidiary role in the E-W extension of the plateau (Yin et al., 1999; Taylor et al., 2003; Taylor and An, 2009; Han et al., 2018). The late Quaternary slip rate of corresponding normal faults is mostly limited to 0.3~0.7 mm/a (Blisniuk and Sharp, 2003; Wu et al., 2015; Li et al., 2019).

In central Tibet, NS-trending normal faults are kinematically linked with and subsidiary to the strike-slip faults. Moderate to large earthquakes are infrequent in central Tibet compared with the high seismicity in plateau margins. However, the Riganpei Co-Yibu Chaka fault-Jiangai Zangbu fault (RYJF) system is an exception recorded several moderate magnitude events since 1973. The ~340km long Riganpei Co fault is a NE-strike left-lateral fault zone, conjugated with the EES-striking Gaize-Dong Co fault, lying on either side of the BNS (Taylor et al., 2003). It starts in Dongcuo Basin in the south, extends NEE~NNE to the pull-apart Yibu Chaka basin, and then connects with the left-slip Jiangai-Zangbu fault on the north side of the basin (Taylor et al., 2003). The Yibu-Chaka graben is characterized by a negative flower structure (Gao et al., 2022) and is divided by a series of NS~NNE-trending normal faults into several fault-bounded tilted blocks and grabens (Figure 2). There are the Gangtang graben, the Heishi range, the Yibu-Chaka graben, the Jiaomu Ri range, the Jiaomu-Chaka graben, and the Birang range from east to west. The range- or graben-bounding normal faults exist always in pairs with opposite dip and same strike, which control together geomorphologic evolution. A variety of late Quaternary features, including pressure ridges, sag ponds, and offset alluvial fans are identified along with the extensional fault system (Taylor et al., 2003). Well-defined offsets of 30-100 meters of these units along the southwestern strike-slip portion of this fault were well-characterized and documented to estimate its Late Quaternary slip rate (Taylor et al., 2003).

Recent moderate magnitude earthquakes of normal type are more frequent in this region. The Nima-Gaize earthquake sequence of $M_s = 6.4, 5.9$, and 5.4 in 2008 occurred in the junction region between the southern end of the Riganpei Co fault and the Gaize-Dong Co fault in southern-central Tibet (Ryder et al., 2010). A three $M_s > 5.3$ moderate earthquake sequence in 1973 occurred in the north of the Yibu-Chaka graben (Molnar and Tapponnier, 1978). The Nima Mw 6.4 earthquake in the center of the Yibu-Chaka graben on 22 July 2020 was the newest and strongest event in the RYJF system.

The epicenter of the 2020 Nima earthquake estimated by the China Earthquake Networks Center (CENC) is 33.19°N, 86.81°E, about 5km from the west of the east-dipping West Yibu-Chaka fault (WYF). However, the epicenter reported by the US Geological Survey (USGS) and GCMT lies almost on the surface projection of the west-dipping East Yibu-Chaka fault (EYF), and about 10km from the east of the WYF. Moreover, a relatively large non-double-couple (non-DC) component of the mainshock included in long-period point-source moment tensor solutions reported in the USGS and GCMT catalogs from 21% to 43% (Table 1 and S1). It may imply this event may not be a pure shearing tectonic earthquake and is associated with geometrically complex shear faulting or combined tensile and shear faulting (Frohlich, 1994; Julian et al., 1998).

Inversion of coseismic and postseismic deformations helps understand the mechanics of fault interaction, the process of postseismic stress transfer, and viscous rheology properties of the lithosphere (Bürgmann and Dresen, 2008). InSAR is an ideal tool to study the 2020 Nima earthquake processing in this extremely remote part of Tibet, where other types of observation are difficult to implement. Several studies from InSAR data have suggested that the Nima earthquake occurred on the WYF (Li et al., 2021; Yang et al., 2021), but others showed different conclusions (Ji et al., 2021; Gao et al., 2022). Moreover, the cause of the afterslip in the Yibu-Chaka graben also remains disputed. Yang et al. (2021) suggested that the postseismic deformation was dominated by aseismic slip, which is inconsistent with the result of slow slip on a fault to the west of the mainshock fault suggested by Gao et al. (Gao et al., 2022). Therefore, we inverted jointly continuous GNSS observations and Sentinel-1 C-band Synthetic Aperture Radar (C-SAR) datasets to determine the coseismic and postseismic slip distributions associated with the 2020 Nima event. Furthermore, we calculated the Coulomb failure stress change (ΔCFS) due to coseismic slip and afterslip. Finally, we attempted to investigate fault interaction during the event, the relationship between afterslip and aftershocks, as well as the mechanics of postseismic deformation.

2 Materials and Methods

The study area is located in the central Tibetan Plateau with an average altitude of greater than 4300m. This area has very few seismic and GNSS observation stations due to limited accessibility. Three continuous GNSS stations within 50 km of the epicenter (Figures 1 and 2) are deployed in 2018 under a collaboration between Tianjin University (led by Jing Liu-Zeng) and Institute of Geology, China Earthquake Administration. One of the GNSS stations, named ROMA and station (86.88°E, 33.15°N) is just around the epicenter and recorded ideally coseismic and postseismic displacement signals. Moreover, the rich high-resolution Sentinel-1A C-band SAR data coverage of the 2020 Nima earthquake, combined with an arid climate and poor vegetation cover, provides a valuable opportunity to illuminate the geometry and interaction of the complex fault system associated with this event. Here, we select 43 ascending and 58 descending track C-SAR image pairs including 2 images on 14 and 18 July 2020, and 99 images from 26 July 2020 to 28 April 2021 for modeling coseismic and postseismic deformation fields (detailed information listed in Table S2).

2.1 GNSS Data Processing

All original RINEX files of GNSS observations are processed initially using GAMIT/GLOBK processing software to separate irrelevant signals and obtain GNSS displacement time series. RINEX files of three continuous GNSS stations and other stable IGS stations in the surrounding area were computed jointly and resulted in a regional single-day coordinate solution. The solution includes several parameter values, such as pole-shift, troposphere phase delay, Earth tide, and their equation-covariance estimation. Then, the regional solution was combined with the global solution obtained

from SOPAC (<http://sopac.ucsd.edu>) using a sequential Kalman filter based on the GLOBK software. Lastly, we convert the combined single-day solution into seven parameters via 50 global service stations to obtain the transformation parameters and convert single-day solutions without reference frame into the coordinate time series within the ITRF 2008 network.

The final ITRF2008 solution $X(t)$ includes long-term tectonic displacement signals, noise associated with seasonal changes, and step signals caused by antenna replacement and earthquakes. The combination signals can be written as follows:

$$X(t) = A \ln \left(1 + \frac{t-t_0}{\tau} \right) + B(t) + C_1 \sin(2\pi t) + C_2 \cos(2\pi t) + C_3 \sin(4\pi t) + C_4 \cos(4\pi t) + \sum_{i=1}^N D_i H(t) \quad (1)$$

In Eq.1, $A \ln(1 + (t - t_0)/t_0)$ represents post-seismic deformation; B is the linear rate of long-term tectonic movement; C_i ($i = 1, 2, 3, 4$) describes noise associated with seasonal changes; $H(t)$ and D_i respectively are instrument step functions and the signal generated by permanent seismic displacement. To separate the post-seismic deformation from the long-term tectonic strain and seasonal noise, we use the least square method to fit the original coordinate time series according to Eq.1 and derive a corrected time series shown in Figure 3 and Table S2.

2.2 Coseismic InSAR Processing

The mature two-pass differential InSAR approach is adopted based on the open-source GMTSAR software (<https://topex.ucsd.edu/gmtsar/>). The whole InSAR processing is performed in a standard procedure way. (1) We adopt a multi-look factor of 20:4 in the range and azimuth direction for the radar data to improve the deformation field SNR and remove system noise. (2) We remove the orbit error and topographic phase using POD files and the 1-arcsec (~30m) resolution DEM from the Shuttle Radar Topography Mission (SRTM) (Farr and Kobrick, 2000). (3) Interferograms were filtered and unwrapped respectively via the Goldstein filtering method (Goldstein and Werner, 1998) and the least-cost flow unwrapping method (Curtis et al., 2001). (4) Interferograms were geocoded into the WGS84 coordinate system. (5) Tropospheric delay is removed via the GACOS model. (6) Residual errors were removed by a linear fitting according to a one-dimensional covariance relation. Besides, some decorrelation regions in the interferograms associated with the Yibu Chaka lake and Jiangai Zangbu river water cover are masked. Figures S1~S3 show the results of the intermediate processes. The T0121A coseismic deformation gradient is significantly greater than that of the T121D at the transition section from the western to the center (Figure 4(e)). Similar patterns also exist in the postseismic time-series deformation of the 2020 Nima earthquake and the coseismic deformation of the 2021 Shuanghu earthquake (Xia et al., 2022). It suggests that the observing view of descending tracks is almost parallel to the long axis of interferograms, not all deformation can be observed, and only a few may be captured.

2.3 Postseismic InSAR Processing

LiCSAR is an open-source Sentinel-1 SAR data automatic processing system developed by (Lazecky et al., 2020) (<https://comet.nerc.ac.uk/COMET-LiCS-portal>), providing interferograms and unwrapping phase data after initial registration. Based on 41 interferograms of T012A and 56 interferograms of T121D compiled by LiCSAR nine months after the mainshock, we construct two groups of Spatio-temporal interference networks by the LiCSBAS method (Morishita et al., 2020) (Figure 5).

The processing of postseismic interferograms is identical to the coseismic interferogram processing. According to a 20:4 ratio of azimuth and distance direction, interferograms with 80m spatial resolution are obtained by multi-look processing. After GACOS atmospheric correction, the standard deviation of interferograms relative to the raw pixel phase is reduced by 20-30%, so processed interferograms are more reliable (Figure 5). Postseismic time-series deformation and deformation rate are derived by the SBAS method in the following steps.

(1) To check interferogram quality, we count firstly the average coherence coefficient of all interferograms as a threshold value, and then data with serious incoherence caused by vegetation and river, or with low coherence coefficients below the threshold value, are masked from interferograms.

(2) Phase unwrapping errors may cause serious deviations to SBAS inversion results, but cannot be identified only by a single interferogram. Thus, it is necessary to identify and remove phase unwrapping errors as possible before inversion. For check phase closure (M. et al., 1988), multi-temporal interferograms are used to identify phase unwrapping errors according to the phase closure principle, and then interferograms that do not meet the error threshold are masked from the data set to be processed.

(3) We carry out the SBAS inversion and estimate the standard deviation between observed values and model values with the Bootstrap method (Efron and Tibshirani, 1986). A high standard deviation implies that some noise or nonlinear deformation is still not removed from data sets.

(5) To avoid noise pixels in the time-series results, the deformation sequences are masked according to the coherence and standard deviation thresholds to be set.

(6) The masked results may still contain errors independent in the time domain but correlated in the space domain, such as residual tropospheric delay errors, ionospheric errors, track errors, etc. Such spatio-temporal dependent (STD) failure situation can be evaluated with a Spatio-Temporal Consistency equation (STC),

$$STC = \min \frac{\lambda}{4\pi} \sqrt{\frac{1}{N-1} \sum_{n=1}^{N-1} ((\phi_R^n - \phi_p^n) - (\phi_R^{n+1} - \phi_p^{n+1}))^2} \quad (2)$$

In Eq.2, λ is radar wavelength; N is the number of interferograms; ϕ is the interference unwrapping phase; R is the distance starting from the coherent pixel point. Eq.2 indicates that the STC is the minimum root mean square (RMS) error of the double difference between the interest coherent point and all of its surrounding coherent points with an R distance in the temporal and spatial domains.

According to the STC value, high-pass and low-pass filtering operations are performed on time-series masked results for obtaining a further reliable result, including one-dimensional and two-dimensional Gaussian kernel filtering in the time domain and space domain, respectively. If the deformation range is enough small relative to the scope of the study area, it is necessary to remove phase ramps via linear or nonlinear regression equations. Figures S4~S7 show the results of the above processes.

Almost no effective deformation is derived from the sixth month after the mainshock. Here, we show the derived results within five months after the mainshock in Figures 6 and Figure S10. The corrected phase standard deviation of interferograms in Figure S5 decreases obviously after atmospheric delay correction with the GACOS model. The STC distribution shown in Figure S9 reported that spatio-temporal discontinuities mainly occurred around the Yibu Chaka lake and agree with the error range

of the STD failure and phase closure. So, filtering operations in Spatio-temporal domains is necessary.

2.4 Verification of Postseismic Deformation

We used the time series of Roma station (Point 1 in Figure 6) near the epicenter as the reference position to verify the postseismic motions derived from InSAR data. We extracted postseismic displacement sequences of three sample points (Points 1, 2, and 3 in Figure 6) and Profile AB, to compare with the GNSS and InSAR displacement sequences, respectively. Here a logarithmic empirical formula (Eq.3) is used to fit the afterslip deformation sequences from InSAR and GNSS methods respectively.

$$X(t) = A \ln \left(1 + \frac{t-t_0}{\tau} \right) \quad (3)$$

In Eq.3, A represents afterslip amplitude; t is the time series after the mainshock (t_0); τ describes the attenuation time of afterslip signs. The final results of Point 1~3 are shown in Figures 7 and S8, which shows the GNSS and InSAR postseismic displacement sequences within nine months after the mainshock was in good agreement with each other. As the observation view of the descending orbit is roughly parallel to the fault, the weak nonlinear deformation signs for descending orbit datasets are dropped even further during the Spatio-temporal filtering processing. In general, high consistency between GNSS and InSAR datasets suggests that the filtered deformation sequences are reliable.

3 Results

3.1 Coseismic Slip Distribution

In addition, the processed coseismic interferograms and deformation fields of T012A and T121D are shown in Figure 4(a)-(d), which reveal perceptible deformation signals in a typical graben structure. Coseismic deformation is observed over an area of about 40km × 30km. The deformation signals for two interferograms both show a slight asymmetric pattern of three obvious lobes, which are slight left-hand columns along the N-E direction. In the ascending and descending interferograms, the central lobe with the highest deformation gradients has a maximum negative LOS displacement value of -29cm and -24cm for T012A and T121D, respectively (negative LOS value represents away from the satellite), and thus with a dominant vertical component. The east and west lobes are in the opposite direction and are different in displacement size, and the former was close to the central lobe in the ascending track and far from the central lobe in the descending track, which indicates the westward has an NWW-direction horizontal motion and the eastward might move slightly to the east.

All reported mainshock epicenters in Table 1 are located in the center lobe. The reported aftershocks fanned out towards the north and are symmetric on the opposite side of the WYF (Figure 2). There is no obvious surface rupture observed which then makes it difficult to directly ascertain the causative fault. The WYF and EYF became possible candidates for this event (Li et al., 2021; Liu et al., 2021; Yang et al., 2021; Gao et al., 2022). To determine the geometry parameters of the seismogenic fault and investigate coseismic and postseismic deformation, a coseismic slip model was inverted jointly using InSAR and GNSS displacement datasets with the same inversion method in the (Wang et al., 2011). Based on the suppose of a homogeneous elastic half-space (Okada, 1985), each fault plane was subdivided into an array of rectangular patches 1 km×1 km and Green's functions for geodetic displacements from the uniform slip on each patch are computed by the PSCMP code (Wang et al., 2006) and the Crust 1.0 model. We carry out a nonlinear inversion algorithm with multiple Monte

Carlo methods to search automatically for an optimal uniform slip model (Table 1). Detailed inversion procedures are described in (Xia et al., 2022).

We check multiple alternative faults and slip models. We set firstly initial parameters of the source models with west-directed dips in 5° intervals between 30° to 70° , resulting in a small fitting degree of 30.3% and a rake of -180° . This result implies that the focus mechanism is pure strike-slip and incompatible with the regional tectonic background and the focus mechanism solutions from the CENC, GCMT, and USGS catalogs. As a result, we prefer to rule out the west-dipping EYF responsible for the mainshock. In turn, we refer to the WYF to set initial parameters with the rake varying from -90° to 20° and the dip between 30° to 90° . The RMS misfit between the model and interferograms decreases with increasing dip, but the improvement is imperceptible for dips above 50° , and a corresponding rake of $\sim 70^\circ$ with a not too high correlation coefficient of 88%. With the epicenter as the boundary, as the north trace of the WYF is adjusted parallelly toward the west up to about 5km, the misfit between observed and model data decays rapidly, and the optimal correlation coefficient is up to 99% (Table 1). Figure 9 shows the optimal result with the largest correlation between observed and model data and the smallest misfit value, with the peak slip of 1.16 m at a depth of 8.4 km. Assuming a shear modulus of 30 GPa, the calculated seismic moment tensor is $6.4 \times 10^{18} \text{ N} \cdot \text{m}$, equivalent to Mw 6.4.

3.2 Postseismic Slip Distribution

To investigate postseismic and the process of postseismic stress transfer, more frequent temporal sampling of the SAR acquisitions is needed. The postseismic slip model is also derived jointly from postseismic InSAR and GNSS displacement datasets (Figure 9). The cumulative afterslip moment within nine months after the mainshock is $1.0 \times 10^{18} \text{ N} \cdot \text{m}$, about 15.6% of that released by the mainshock. It is consistent with the estimated results based on typical crustal earthquake sequences (Kagan and Houston, 2005).

3.3 Coseismic and Postseismic Coulomb Stress Change

To investigate the process of postseismic stress transfer and the relationship between afterslip and aftershocks, we calculated coseismic and postseismic ΔCFS s based on a biviscous Burgers body with the friction coefficient of 0.4, Young's modulus of 30 GPa, Poisson's ratio of 0.25, and the InSAR-derived node plane solution (Table 1, Figure S9). According to the Coulomb instability criterion, we calculated coseismic and postseismic ΔCFS s at depths of 2 km, 4 km, 10 km, 16 km, 18 km, and 20 km (Figure 10, 11), as well as the coseismic ΔCFS along the upper wall of the seismogenic fault with depth (Figure 12).

4 Discussion

4.1 The Seismogenic Fault and Fault Interaction

As shown in Figure 13, our InSAR-derived coseismic slip model suggests a complex reversed “S-shape” composite structure at fault junctions, with an overall trend of $\text{N}28^\circ\text{E}$, which is well consistent with the orientation of region existing geologic structures and the region shearing stress direction (Taylor et al., 2003). From table 1, all of the dip angles of the seismogenic fault from seismic and geodetic inversions are greater than 48° . It hints the rheological structure may differ from that in southern Tibet, related to the low-angle subduction of the Indian Plate under the Eurasian Plate (Zhao et al., 2017).

Toward the south of the epicenter, Segment AC in Figure 13 stretches about 18km almost along the mapped N35°E-striking WYF associated with sharp fault morphology (Molnar and Tapponnier, 1978). Then, near the epicenter, the earthquake rupture didn't go on along the WYF and rotated by about 20° to the north. The results lead to a fault bend of ~5km (Segment CD in Figure 12) near where the WYF and the HF intersect. On the bend, the source rupture initially developed and then was up to the peak of 1.16m at the depth of 8.4 km, which might result from stress localization in such a relatively weak material condition (Dayem et al., 2009). The shear direction was rotated by near-field dynamic stress during the earthquake rupture process and led to an angle of ~20° over the WYF.

To the north, the earthquake rupture caused a rotation of ~25°, turn back to the N40°E direction, and keeps on toward the North about 20km (Segment DB in Figure 12) but not along with the northern segment of the WYF. Segment DB is an unmapped fault about 5km from and parallel to the northern segment of WYF, different from the WYF associated with sharp scarps, and buried under the unconsolidated Holocene alluvium of the Nanliu and Jiangai-Zangbu rivers. On account of long-term reorientation of stresses because of strain accumulation, construction complexity, and so on, the stress field around mature fault zones is often misaligned with existing faults (Preuss et al., 2019), and then promotes the reactivation of inactive and potentially blind or unknown branches. Considering Segment DB is located in the hanging wall of the WYF away from the central graben, we suggest that it is likely to be a younger blind fault parallel to the remote stress field.

More than one fault ruptured during this earthquake, which hinted the rupture process is complex and included possibly two actions: the inherited effect of the preexisting WYF and the dynamic-triggering effect of the blind fault. Aftershocks distribution is not a band pattern along the seismogenic fault but a fan with the center axis of the seismogenic fault. Such a fan pattern is generally consistent with the lateral extension range of the negative flower structure of the Yibu-Chaka graben, it also hints that the relaxation process during this event may be dominated by multi-fault interaction. The non-double-couple component reflects the complexity of the focal mechanism (Zhu and Ben-Zion, 2013). When shearing ruptures of intersected faulting planes are not parallel to each other with different geometry and could result in a composite torsional shear and tensile fracture component (Julian et al., 1998), and then lead to the larger non-DC component in the long-period point-source solutions (Table 1). In short, our coseismic slip distribution provided a more refined resolution of the rupture trace of this earthquake, which is crucial to understanding the mechanism of earthquake rupture and fault interaction.

4.2 The Mechanics of Postseismic Deformation

The spatiotemporal distribution of afterslip provides important clues to the mechanism of afterslip. The postseismic slip distribution was complementary to the coseismic slip distribution in space (Wallace et al., 2018) and shows a 42cm peak slip at the up-dip shallow depth of ~4 km and a 31cm peak slip at the downdip deep depth of ~16 km of the coseismic rupture zone, respectively (Figure 9). Figures 10 and 11 show quantitatively coseismic and postseismic Δ CFS at different depths during the mainshock and aftershocks. Coseismic and postseismic Δ CFSs along Segment AC are generally reduced, this suggests the accumulated stress along the segment is fully released. Along Segment CD, coseismic Δ CFS is obviously increased except near the focal depth, and postseismic stress is weakly positive only within the depth of 10~16km. For Segment DB, coseismic stresses at different depths are increased except near the focal depth and are mostly released during the postseismic process. The coseismic Δ CFS along the EYF is increased in a narrow and long belt at relatively shallow and deep depths, and the stress after the mainshock is only increased at the depth of around

16-18km. The early 8-day aftershocks after the mainshock were mostly distributed within about 15 km of the epicenter and completely located in the shadow patch of the InSAR-derived coseismic Δ CFS at the depth of ~ 10 km. The latter aftershocks gradually migrate to the northwest and northeast over time and were observed within a more wide region of ~ 36 km from the epicenter. It indicates a dynamic releasing process of postseismic stress.

The net moment release associated with afterslip within the first nine months after the mainshock, amounted to $\sim 15.6\%$ of that of the mainshock. It indicates afterslips have mostly contributed to the release of additional seismic energy. The negative patch of coseismic Δ CFS at the depth of 10km and positive patches of Δ CFSs at shallow depths of < 10 km have good coherence to aftershock distribution. However, it is worth noting that around the source, there are two positive postseismic Δ CFS patches of > 1 bar in up-dip and downdip parts of the coseismic slip zone at depth of 4km and > 16 km, respectively (Figure 13). Around the region projected onto the surface by the up-dip part, Li et al. found some tectonic extension cracks and surface breaks related to surface shaking (Li et al., 2021). The slight shallow coseismic dip-slip near 40km along the seismogenic fault was almost close to the surface. Hence, we prefer to suggest that shallow creep at the depth of ~ 4 km could be facilitated by stress perturbations.

In the vicinity of the positive postseismic Δ CFS patches along the EYF at > 16 km, there was a slight uplift in the afterslip distribution. The focus depth determined by body wave modeling is 10 km (Table 1), and all aftershocks were located in the shallow crust of < 10 km (Figure 9). The rupture depth of this earthquake is larger than the effective viscoelastic layer thickness of ~ 10 km in central Tibet (England et al., 2013; Liu-Zeng et al., 2020) and the long-term equivalent elastic thickness of 10 \sim 12 km in the Tibetan plateau (Molnar and Chen, 1983; Molnar and Lyon-Caen, 1989; Chu et al., 2009). We assume the reactivation of the conjugate EYF with the WYF could be promoted by this event and then followed by the adjustment of the stress field surrounding faults.

The deformation source extends further down the brittle coseismic rupture, which has implications for the rheology of downdip extension of the dipping faults or shear zones in southern Tibet (England et al., 2013; Liu-Zeng et al., 2020) and provides clues to the rheological properties of the lower crust of the Tibetan plateau (Shi et al., 2012; England et al., 2013). The interaction of multiple faults is through stress transfer, which can promote seismic hazards within years after an earthquake (Jia et al., 2021). The Δ CFSs on the EYF and Segment CB increase more than 1 bar, which encourages paying further refined attention to the normal fault (Li et al., 2021). The transition zone joined with the tail end of the left-lateral Riganpei Co and Jiangai Zangbu faults deserve especially longer-term afterslip observation over timescales of years.

5 Conclusions

We invert jointly the coseismic and postseismic deformation sequence of the 2020 Nima earthquake using InSAR and GNSS displacement datasets within the first nine months after the mainshock. Our results suggest the Nima earthquake ruptured a complex reversed “S-shape” composite structure at fault junctions with a moderate dip angle of 50° , which is different from normal faults in southern Tibet with low dip angles. This earthquake rupture process was complex and ruptured more than one fault, including at least the West Yibu-Chaka fault, the junction of the West Yibu-Chaka fault and Heishi fault, and an unmapped younger blind fault parallel to the West Yibu-Chaka fault and promoted to reactivation of the East Yibu-Chaka. Interaction of multiple intersection faults may account for the larger non-DC component in the long-period point-source solutions. From the coseismic and postseismic coulomb failure stress changes, the concentrated stress at the shallow

depth of <10 km was released mainly by the mainshock and aftershocks. The shallow creep at the depth of ~4 km around the intermediate region between the northern segment of the West Yibu-Chaka fault and the adjacent blind fault could be facilitated by stress perturbations. The deep afterslip of >16 km depth along the East Yibu-Chaka fault extended within the brittle-ductile transition zone of the coseismic rupture zone. It indicates the rheology of down-dip extension of the dipping faults in southern Tibet. The more than 1 bar ΔCFS around the East Yibu-Chaka fault and the northern of the West Yibu-Chaka fault highlights seismic hazards in the region, especially in the transition zones joined with tail ends of the Riganpei Co and Jiangai Zangbu faults. It is necessary to forecast accurately by longer-term afterslip observation over timescales of years for the faults.

Conflict of Interest

The authors declare that the research was conducted in the absence of any commercial or financial relationships that could be construed as a potential conflict of interest.

Author Contributions

X.L. and J.L.-Z. conceived and designed the experiments; X.L., T.X., and D.D. performed the experiments; T.X. and P.Y. analyzed the InSAR data; Z.J., P.W., and W.W. analyzed the GNSS data; X.L. wrote the paper, and all co-authors contributed to the writing. All authors have read and agreed to the published version of the manuscript.

Funding

Science for Earthquake Resilience, China Earthquake Administration (XH221705C), This work is supported by the National Natural Science Foundation of China (U1839203, 42011540385).

Acknowledgments

Our thanks go to Teng Wang, Minhan Sheng, Guixi Yi, Changsheng Jiang, Shengle Li, Hongwei Tu, Guichun Wei and Wei Wang for their help and discussions. All Sentinel-1A SAR data are copyrighted by the European Space Agency. Atmospheric corrected data were downloaded from the Generic Atmospheric Correction Online Service for InSAR. Most figures were made using the public domain Generic Mapping Tools (Wessel and Smith, 1998).

References

- Armijo, R., Tapponnier, P., and Han, T. (1989). Late Cenozoic right-lateral strike-slip faulting in southern Tibet. *Journal of Geophysical Research: Solid Earth* 94(B3), 2787-2838. doi: <https://doi.org/10.1029/JB094iB03p02787>.
- Blisniuk, P.M., and Sharp, W.D. (2003). Rates of late Quaternary normal faulting in central Tibet from U-series dating of pedogenic carbonate in displaced fluvial gravel deposits. *Earth & Planetary Science Letters* 215(1-2), 169-186.
- Bürgmann, R., and Dresen, G. (2008). Rheology of the Lower Crust and Upper Mantle: Evidence from Rock Mechanics, Geodesy, and Field Observations. *Annual Review of Earth and Planetary Sciences* 36(1), 531-567. doi: 10.1146/annurev.earth.36.031207.124326.
- Chevalier, M.-L., Tapponnier, P., van der Woerd, J., Leloup, P.H., Wang, S., Pan, J., et al. (2020). Late Quaternary Extension Rates Across the Northern Half of the Yadong-Gulu Rift:

Implication for East-West Extension in Southern Tibet. *Journal of Geophysical Research: Solid Earth* 125(7), e2019JB019106. doi: <https://doi.org/10.1029/2019JB019106>.

Chu, R., Zhu, L., and Helmberger, D.V. (2009). Determination of earthquake focal depths and source time functions in central Asia using teleseismic P waveforms. *Geophysical Research Letters* 36(17). doi: <https://doi.org/10.1029/2009GL039494>.

Curtis, W., Chen, Howard, A., and Zebker (2001). Network approaches to two-dimensional phase unwrapping: intractability and two new algorithms: erratum. *Journal of the Optical Society of America A* 18(5), 1192-1192.

Dayem, K.E., Houseman, G.A., and Molnar, P. (2009). Localization of shear along a lithospheric strength discontinuity: Application of a continuous deformation model to the boundary between Tibet and the Tarim Basin. *Tectonics* 28(3). doi: <https://doi.org/10.1029/2008TC002264>.

Efron, B., and Tibshirani, R. (1986). Bootstrap Methods for Standard Errors, Confidence Intervals, and Other Measures of Statistical Accuracy. *Statistical Science* 1, 54-75.

Elliott, J.R., Walters, R.J., England, P.C., Jackson, J.A., Li, Z., and Parsons, B. (2010). Extension on the Tibetan plateau: recent normal faulting measured by InSAR and body wave seismology. *Geophysical Journal International* 183(2), 503-535. doi: 10.1111/j.1365-246X.2010.04754.x.

England, P.C., Walker, R.T., Fu, B., and Floyd, M.A. (2013). A bound on the viscosity of the Tibetan crust from the horizontality of palaeolake shorelines. *Earth and Planetary Science Letters* 375, 44-56. doi: <https://doi.org/10.1016/j.epsl.2013.05.001>.

Farr, T.G., and Kobrick, M. (2000). Shuttle radar topography mission produces a wealth of data. *Eos, Transactions American Geophysical Union* 81(48), 583-585. doi: <https://doi.org/10.1029/EO081i048p00583>.

Frohlich, C. (1994). Earthquakes with non-double-couple mechanisms. *Science* 264(5160), 804-809.

Gao, H., Liao, M., Liang, X., Feng, G., and Wang, G. (2022). Coseismic and Postseismic Fault Kinematics of the July 22, 2020, Nima (Tibet) Ms6.6 Earthquake: Implications of the Forming Mechanism of the Active N-S-Trending Grabens in Qiangtang, Tibet. *Tectonics* 41(3), e2021TC006949. doi: <https://doi.org/10.1029/2021TC006949>.

Goldstein, R.M., and Werner, C.L. (1998). Radar interferogram filtering for geophysical applications. *Geophysical Research Letters* 25(21), 4035-4038.

Ha, G., Wu, Z., and Liu, F. (2019). Late Quaternary vertical slip rates along the Southern Yadong–Gulu Rift, Southern Tibetan Plateau. *Tectonophysics*.

Han, S., Li, H., Pan, J., Lu, H., Zheng, Y., Liu, D., et al. (2018). Co-seismic surface ruptures in Qiangtang Terrane: Insight into Late Cenozoic deformation of central Tibet. *Tectonophysics* 750.

Harrison, T.M., Copeland, P., Kidd, W.S.F., and Lovera, O.M. (1995). Activation of the Nyainqentanghla Shear Zone: Implications for uplift of the southern Tibetan Plateau. *Tectonics*.

Ji, Z., Zhang, Y., and Wang, S. (2021). Coseismic deformation field and fault slip distribution inversion of the Ms 6.6 Nima, Xizang earthquake by Sentinel-1A InSAR data. *Progress in Geophysics (in Chinese)* (1), 1-10.

- Jia, K., Zhou, S., Zhuang, J., and Jiang, C. (2021). Stress Transfer Along the Western Boundary of the Bayan Har Block on the Tibet Plateau From the 2008 to 2020 Yutian Earthquake Sequence in China. *Geophysical Research Letters* 48, e94125. doi: 10.1029/2021gl094125.
- Julian, B.R., Miller, A.D., and Foulger, G.R. (1998). Non-double-couple earthquakes 1. Theory. *Reviews of Geophysics* 36(4), 525-549. doi: <https://doi.org/10.1029/98RG00716>.
- Kagan, Y.Y., and Houston, H. (2005). Relation between mainshock rupture process and Omori's law for aftershock moment release rate. *Geophysical Journal International* 163(3), 1039-1048. doi: 10.1111/j.1365-246X.2005.02772.x.
- Kapp, P., Taylor, M., Stockli, D., and Ding, L. (2008). Development of active low-angle normal fault systems during orogenic collapse: Insight from Tibet. *Geology* 36(1), 7-10.
- Lazecký, M., Spaans, K., González, P.J., Maghsoudi, Y., Morishita, Y., Albino, F., et al. (2020). LiCSAR: An Automatic InSAR Tool for Measuring and Monitoring Tectonic and Volcanic Activity. *Remote Sensing* 12(15), 2430.
- Li, K., Kirby, E., Xu, X., Chen, G., Ren, J., and Wang, D. (2019). Rates of Holocene normal faulting along the Dong Co fault in central Tibet, based on ¹⁴C dating of displaced fluvial terraces. *Journal of Asian Earth Sciences* 183, 103962. doi: <https://doi.org/10.1016/j.jseaes.2019.103962>.
- Li, K., Li, Y., Tapponnier, P., Xu, X., Li, D., and He, Z. (2021). Joint InSAR and Field Constraints on Faulting During the Mw 6.4, July 23, 2020, Nima/Rongma Earthquake in Central Tibet. *Journal of Geophysical Research: Solid Earth* 126(9), e2021JB022212. doi: <https://doi.org/10.1029/2021JB022212>.
- Liu-Zeng, J., Zhang, Z., Rollins, C., Gualandi, A., Avouac, J.-P., Shi, H., et al. (2020). Postseismic Deformation Following the 2015 Mw7.8 Gorkha (Nepal) Earthquake: New GPS Data, Kinematic and Dynamic Models, and the Roles of Afterslip and Viscoelastic Relaxation. *Journal of Geophysical Research: Solid Earth* 125(9), e2020JB019852. doi: <https://doi.org/10.1029/2020JB019852>.
- Liu, F., Pan, J., Li, H., Sun, Z., Liu, D., Lu, H., et al. (2021). Characteristics of Quaternary Activities along the Riganpei Co Fault and Seismogenic Structure of the July 23, 2020 Mw6.4 Nima Earthquake, Central Tibet. *Acta Geoscientica Sinica* (42), 139-154.
- M., G.R., A., Z.H., and L., W.C. (1988). Satellite radar interferometry: Two-dimensional phase unwrapping. *Radio Science* 23(4), 713-720.
- Molnar, P., and Chen, W.-P. (1983). Focal depths and fault plane solutions of earthquakes under the Tibetan Plateau. *Journal of Geophysical Research: Solid Earth* 88(B2), 1180-1196. doi: <https://doi.org/10.1029/JB088iB02p01180>.
- Molnar, P., and Lyon-Caent, H. (1989). Fault plane solutions of earthquakes and active tectonics of the Tibetan Plateau and its margins. *Geophysical Journal International* 99(1), 123-153. doi: 10.1111/j.1365-246X.1989.tb02020.x.
- Molnar, P., and Tapponnier, P. (1978). Active tectonics of Tibet. *Journal of Geophysical Research: Solid Earth* 83(B11), 5361-5375. doi: <https://doi.org/10.1029/JB083iB11p05361>.
- Morishita, Y., Lazecky, M., Wright, T.J., Weiss, J.R., Elliott, J.R., and Hooper, A. (2020). LiCSBAS: An Open-Source InSAR Time Series Analysis Package Integrated with the LiCSAR Automated Sentinel-1 InSAR Processor. *Remote Sensing* 12(3), 424.

- Okada, Y. (1985). Surface deformation due to shear and tensile faults in a half-space. *Bulletin of the Seismological Society of America* 75, 1135-1154.
- Preuss, S., Herrendörfer, R., Gerya, T., Ampuero, J.-P., and van Dinther, Y. (2019). Seismic and Aseismic Fault Growth Lead to Different Fault Orientations. *Journal of Geophysical Research: Solid Earth* 124(8), 8867-8889. doi: <https://doi.org/10.1029/2019JB017324>.
- Ryder, I., Burgmann, R., and Sun, J. (2010). Tandem afterslip on connected fault planes following the 2008 Nima-Gaize (Tibet) earthquake. *Journal of Geophysical Research: Solid Earth* 115(B3). doi: <https://doi.org/10.1029/2009JB006423>.
- Shi, X., Kirby, E., Furlong, K.P., Wang, E., Meng, K., Phillips, F.M., et al. (2012). Preliminary constraints on rheology of the deep crust beneath central Tibet from Late Pleistocene—Early Holocene shorelines. *Geophys. Res. Abstr* EGU2012-10796(14), 1.
- Tapponnier, P., Zhiqin, X., Roger, F., Meyer, B., Arnaud, N., Wittlinger, G., et al. (2001). Oblique Stepwise Rise and Growth of the Tibet Plateau. *Science* 294(5547), 1671-1677.
- Taylor, M., and An, Y. (2009). Active structures of the Himalayan-Tibetan orogen and their relationships to earthquake distribution, contemporary strain field, and Cenozoic volcanism. *Geosphere* 5(3), 199-214.
- Taylor, M., Yin, A., Ryerson, F.J., Kapp, P., and Ding, L. (2003). Conjugate strike-slip faulting along the Bangong-Nujiang suture zone accommodates coeval east-west extension and north-south shortening in the interior of the Tibetan Plateau. *Tectonics* 22(4). doi: <https://doi.org/10.1029/2002TC001361>.
- Wallace, L.M., Hreinsdóttir, S., Ellis, S., Hamling, I., D'Anastasio, E., and Denys, P. (2018). Triggered Slow Slip and Afterslip on the Southern Hikurangi Subduction Zone Following the Kaikōura Earthquake. *Geophysical Research Letters* 45(10), 4710-4718. doi: <https://doi.org/10.1002/2018GL077385>.
- Wang, H., Elliott, J.R., Craig, T.J., Wright, T.J., Liu-Zeng, J., and Hooper, A. (2014). Normal faulting sequence in the Pumqu-Xainza Rift constrained by InSAR and teleseismic body-wave seismology. *Geochemistry, Geophysics, Geosystems* 15(7), 2947-2963. doi: <https://doi.org/10.1002/2014GC005369>.
- Wang, R., Lorenzo-Martín, F., and Roth, F. (2006). PSGRN/PSCMP—a new code for calculating co- and post-seismic deformation, geoid and gravity changes based on the viscoelastic-gravitational dislocation theory. *Computers & Geosciences* 32(4), 527-541. doi: <https://doi.org/10.1016/j.cageo.2005.08.006>.
- Wang, R., Schurr, B., Milkereit, C., Shao, Z., and Jin, M. (2011). An Improved Automatic Scheme for Empirical Baseline Correction of Digital Strong-Motion Records. *Bulletin of the Seismological Society of America* 101(5), 2029-2044. doi: 10.1785/0120110039.
- Wang, S., Chevalier, M.-L., Pan, J., Bai, M., Li, K., Li, H., et al. (2020). Quantification of the late Quaternary throw rates along the Yadong rift, southern Tibet. *Tectonophysics* 790, 228545. doi: <https://doi.org/10.1016/j.tecto.2020.228545>.
- Wessel, P., and Smith, W. (1998). New, improved version of generic mapping tools released. *Eos Transactions American Geophysical Union* 79(47), 579-579.
- Wu, Z., Long, C., Fan, T., Zhou, C., Feng, H., Yang, Z., et al. (2015). The arc rotational-shear active tectonic system on the southeastern margin of Tibetan Plateau and its dynamic characteristics and mechanism. *Geological Bulletin of China* 34(01), 1-31.

- 540 Xia, T., Liu, X., Yu, P., Deng, D., Yue, Z., and Gao, T. (2022). Coseismic Rupture Model of the
541 2021 Shuanghu M5.7 Earthquake Based on Sentinel-1A. *Journal of Geodesy and*
542 *Geodynamics* 42(5), 533-540.
- 543 Yang, J., Xu, C., Wen, Y., and Xu, G. (2021). The July 2020 Mw 6.3 Nima Earthquake, Central
544 Tibet: A Shallow Normal - Faulting Event Rupturing in a Stepped Zone. *Seismological*
545 *Research Letters* 93(1), 45-55. doi: 10.1785/0220210057.
- 546 Yin, A., Kapp, and Paul, A. (1999). Significant late Neogene east-west extension in northern Tibet.
547 *Geology*.
- 548 Yin, A., and Taylor, M.H. (2011). Mechanics of V-shaped conjugate strike-slip faults and the
549 corresponding continuum mode of continental deformation. *Geological Society of America*
550 *Bulletin* 123(9-10), 1798-1821.
- 551 Zhao, B., Bürgmann, R., Wang, D., Tan, K., Du, R., and Zhang, R. (2017). Dominant Controls of
552 Down-dip Afterslip and Viscous Relaxation on the Postseismic Displacements Following the
553 Mw7.9 Gorkha, Nepal, Earthquake. *Journal of Geophysical Research: Solid Earth* 122(10),
554 8376-8401. doi: <https://doi.org/10.1002/2017JB014366>.
- 555 Zhu, L., and Ben-Zion, Y. (2013). Parametrization of general seismic potency and moment tensors
556 for source inversion of seismic waveform data. *Geophysical Journal International* 194(2),
557 839-843. doi: 10.1093/gji/ggt137.

558

559

Figures and tables

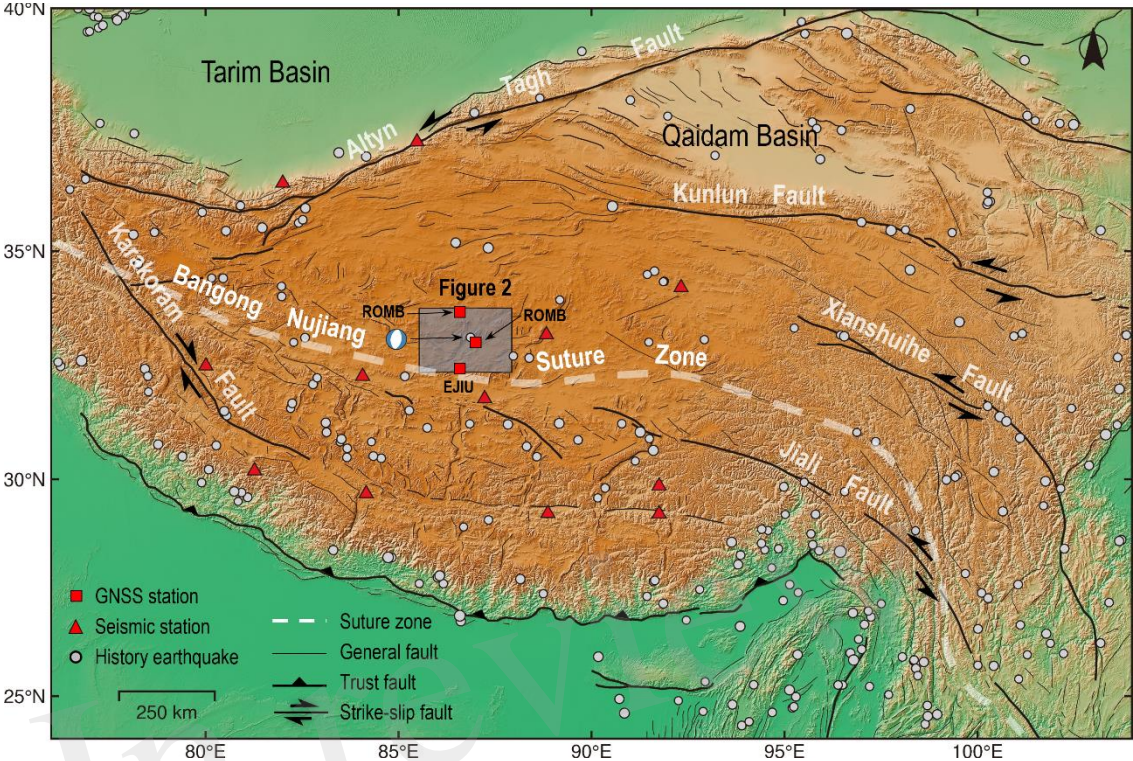


Figure 1. Topographic and tectonic setting map of the Tibetan plateau overlain with earthquakes with magnitude larger than Mw 4.5 from 1 January 1966 to 1 April 2021 from Harvard centroid moment tensor (CMT) catalog. The light-blue earthquake focal mechanism is the epicenter of the 2020 Nima earthquake. Red triangles denote the seismic stations used in this study. Black rectangles depict footprints of this study area. Black lines indicate regional active faults from Tapponnier (Tapponnier et al., 2001). Thrust faults have barbs on the upper plate, arrows indicate the direction of horizontal motion for strike-slip faults. The dashed white line is the Bangong Nujiang suture zone.

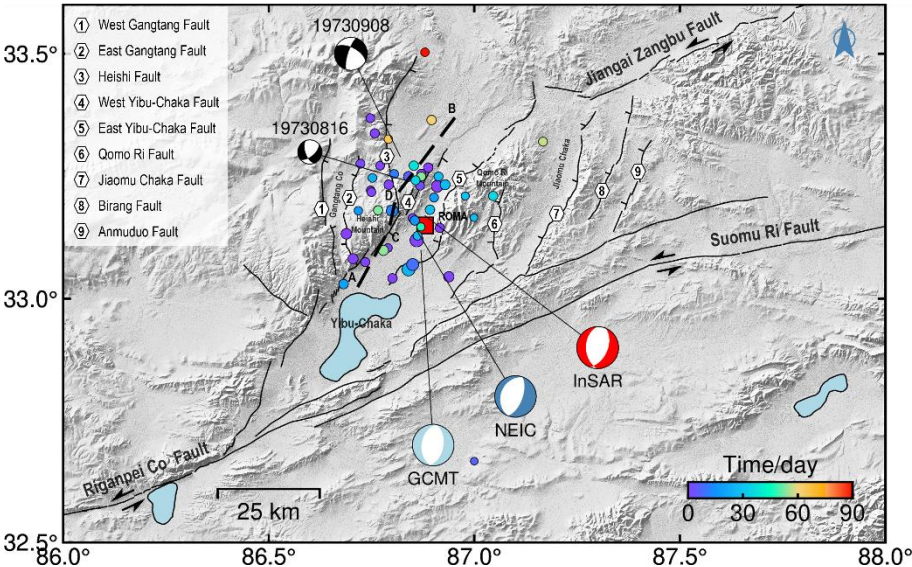
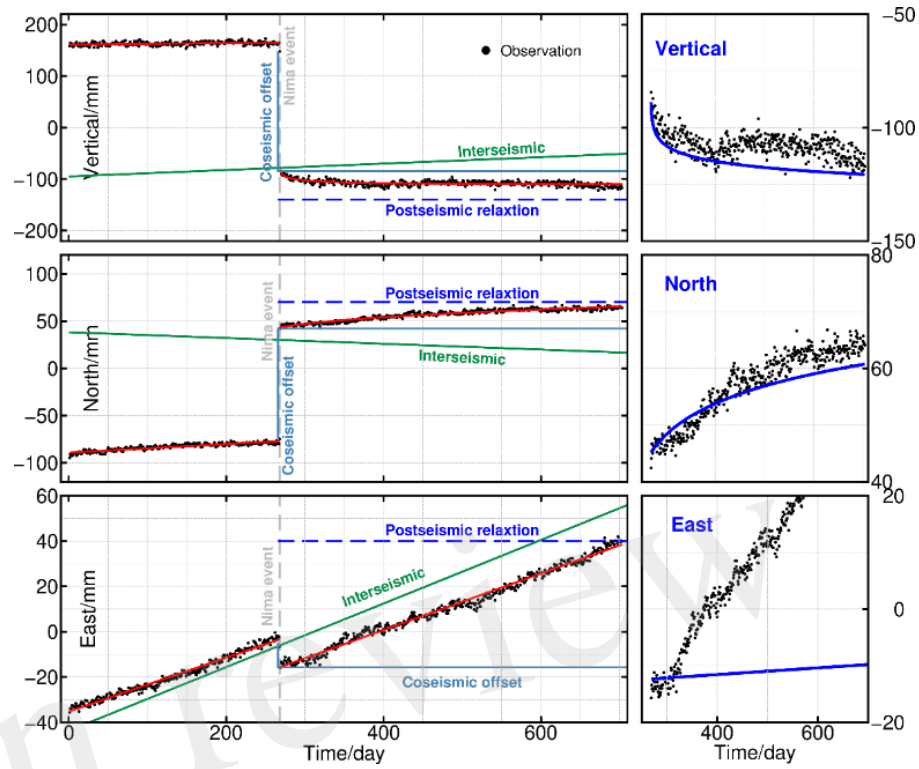


Figure 2. Topographic and tectonic setting map of the Yibu-Chaka graben. Black lines indicate regional active faults modified after Taylor and Yin (Taylor and An, 2009) and interpreted from satellite images. Focal mechanism solutions of the 2020 Nima event from different organizations in Table 3 and three Mw4.5+ aftershocks from the GCMT catalog. Black and white earthquake focal mechanisms are the M>5.0 earthquake in 1973 (Molnar and Tapponnier, 1978). The solid color

573 circles are aftershocks within nine months after the mainshock reported in the CENC ($M \geq 2.7$) catalogs, and the circle sizes
 574 indicate the magnitude of aftershocks. The black dash line is the derived fault trace via the geodetic dataset.



575
 576 **Figure 3.** GNSS time-series signal decomposes in North, East, and Vertical direction for the ROMA station.

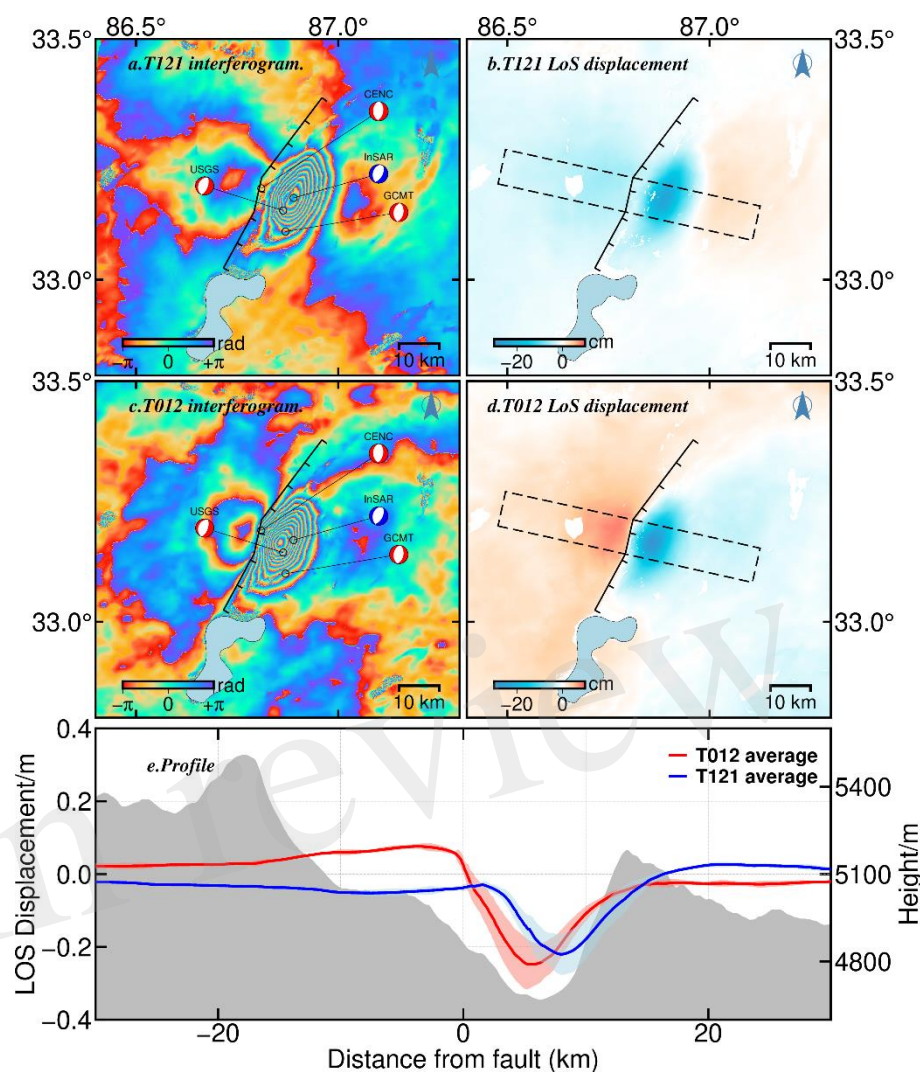


Figure 4. Coseismic deformation of T012A and T121D during the 2020 Nyima earthquake.

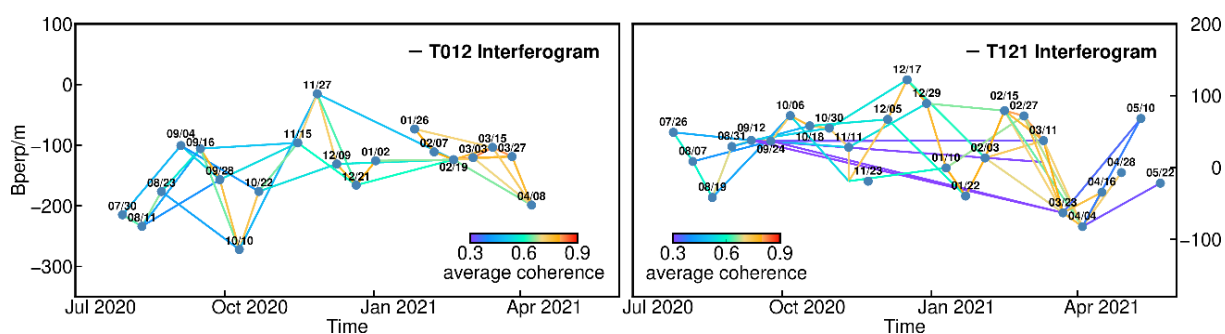


Figure 5. SBAS interferogram network following the 2020 Nyima earthquake.

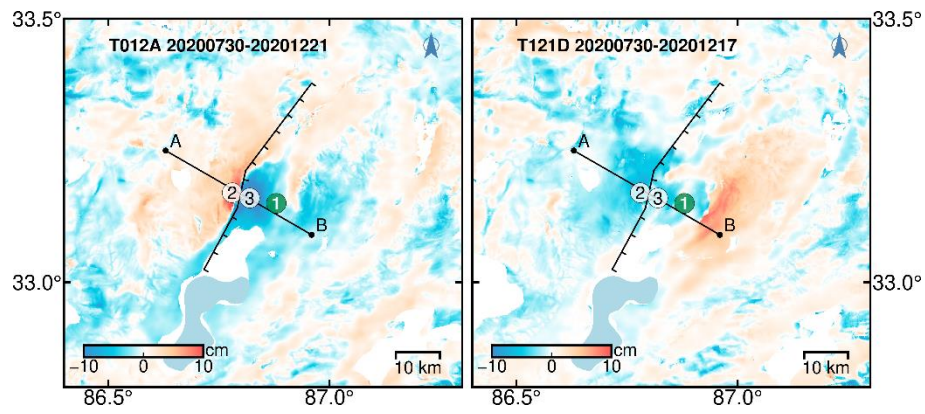


Figure 6. Cumulative deformation five months after the 2020 Nyima earthquake

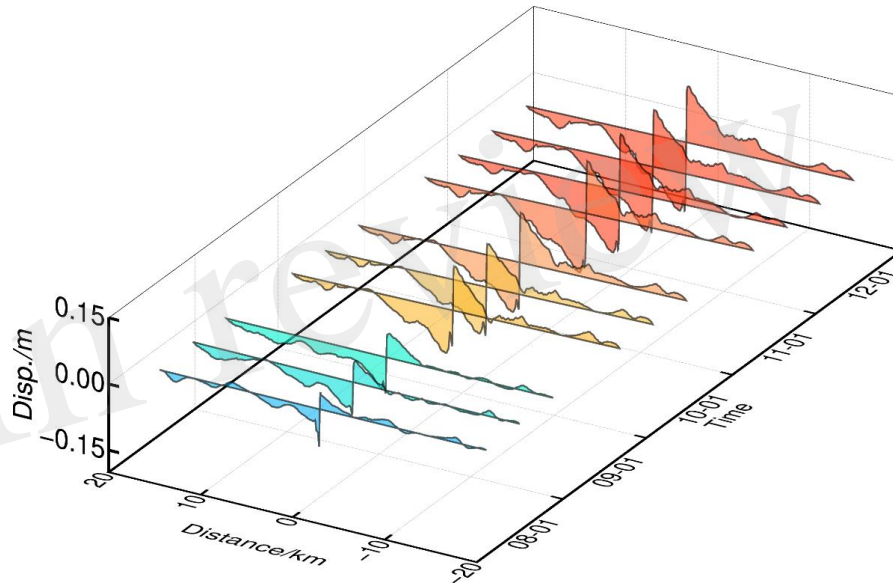


Figure 7. The AB profile sequence of cumulative deformation of Point 1 along the survey line in the direction of ascending track within five months after the 2020 Nima earthquake. The color gradient from blue to red indicates that the deformation amplitude changes from large to small.

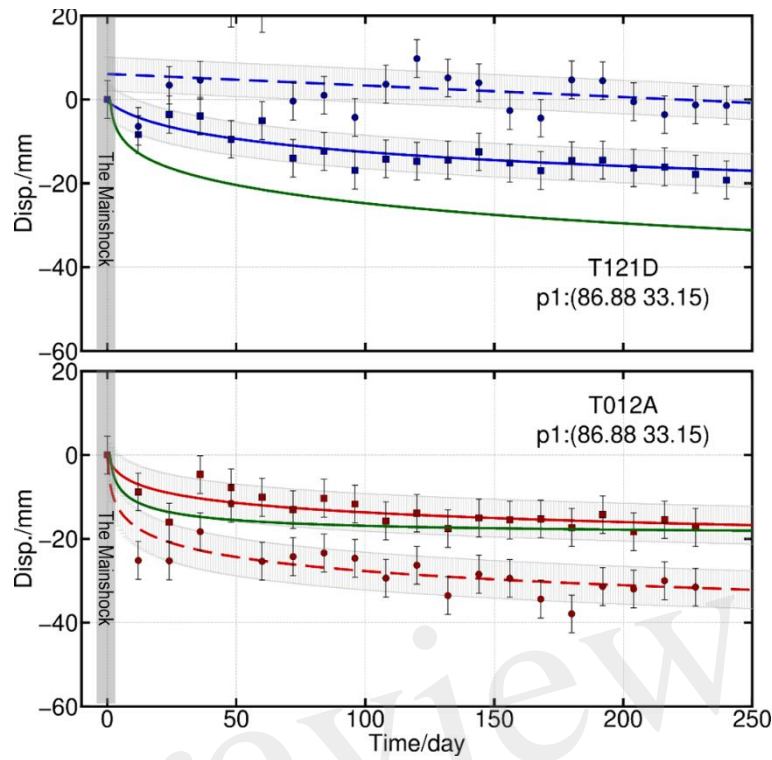


Figure 8. Postseismic displacement sequences at ROMA station within nine months after the mainshock. The green line is the afterslip displacement trace from GNSS datasets projected on the corresponding track direction. The red and blue line traces from ascending and descending track datasets, respectively. Circle/square points, and solid/dashed lines indicate datasets and fitted results before and after Spatio-temporal filtering, respectively.

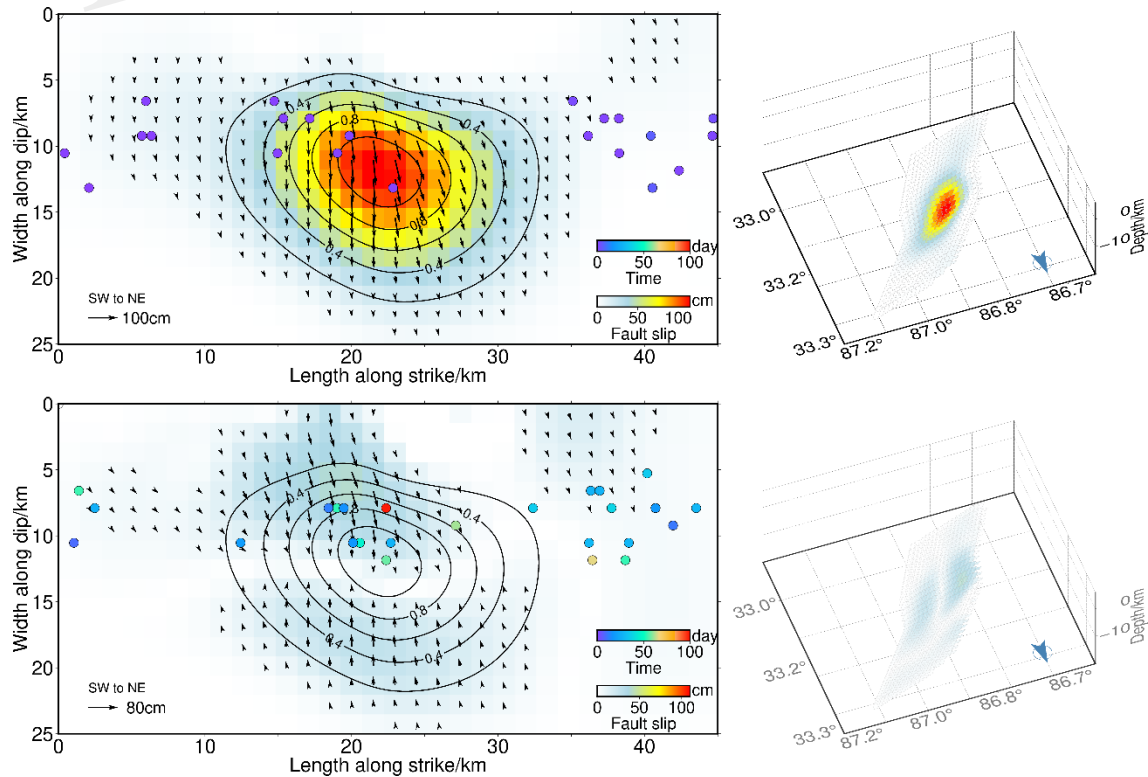


Figure 9. Coseismic and postseismic slip models of the 2020 Nima earthquake. Color circle points indicate aftershocks of the first eight days and latter eight months, respectively.

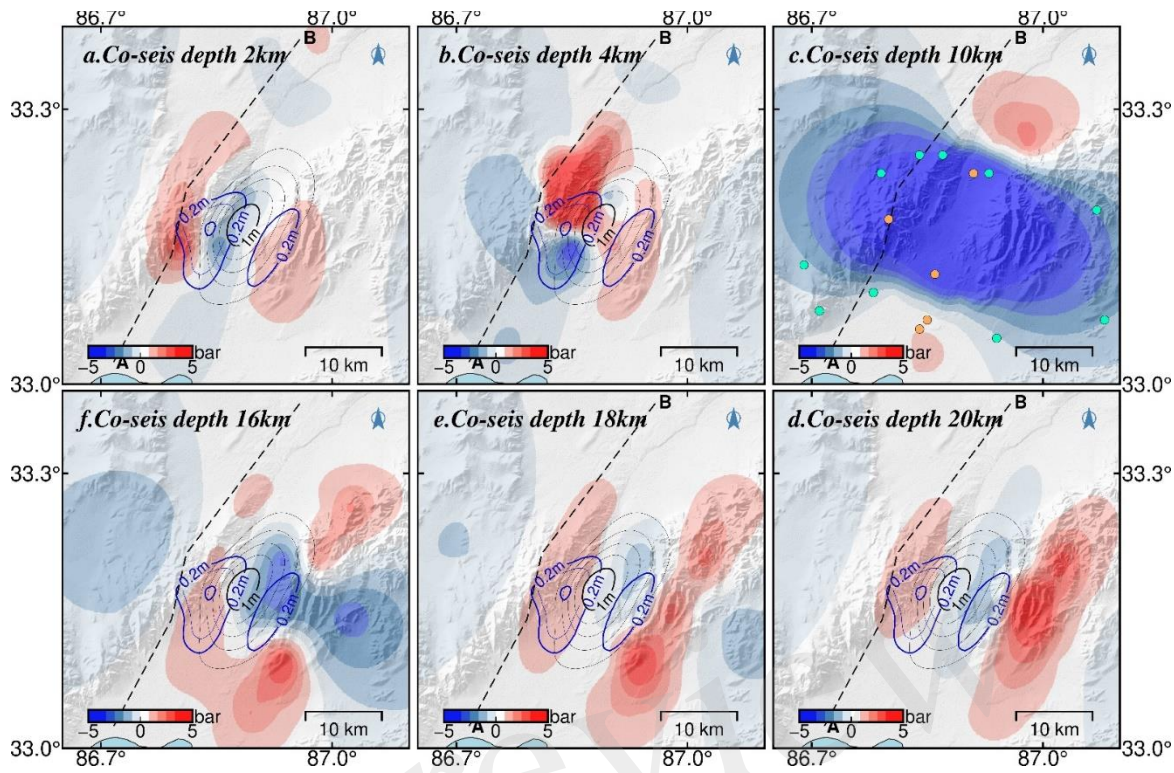


Figure 10. Coseismic Coulomb stress changes of the 2020 Nima earthquake with aftershocks of the first eight days and latter eight months. The blue line is the isoline projected on the surface of residual slip, with an interval of 0.1m. The black line is the isoline projected on the sliding surface of the main earthquake with an interval of 0.2m. The color circles represent $M \geq 3$ aftershocks of the first eight days. The dotted line AB indicates the seismogenic fault.

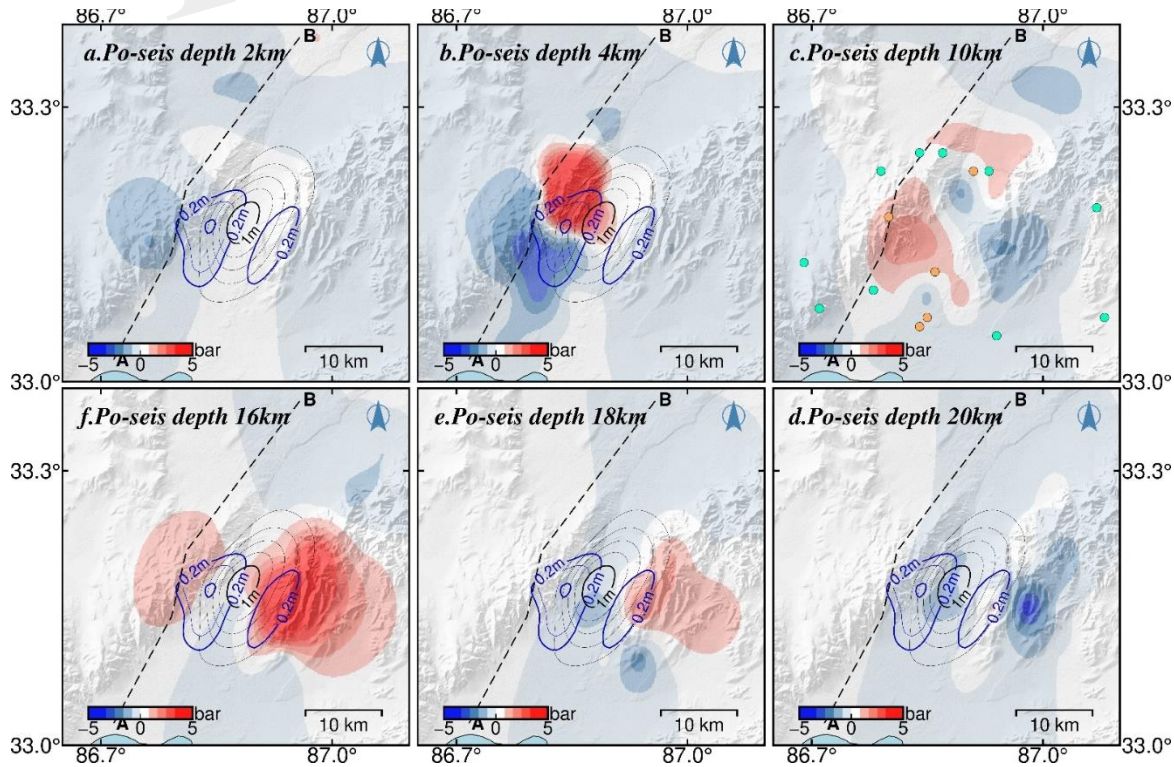


Figure 11. Post-seismic Coulomb stress changes of the 2020 Nima earthquake. Captions are as for Figure 10.

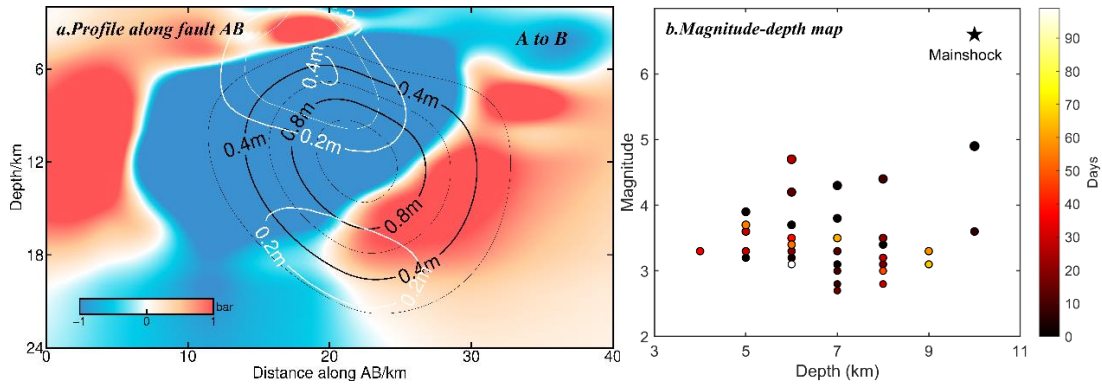


Figure 12. Coseismic Coulomb stress change of Profile AB along depth for the 2020 Nima earthquake and Magnitude & depth map. The black (0.2m interval) and white lines (0.1m interval) are projections on the surface of coseismic and postseismic slip contours, respectively.

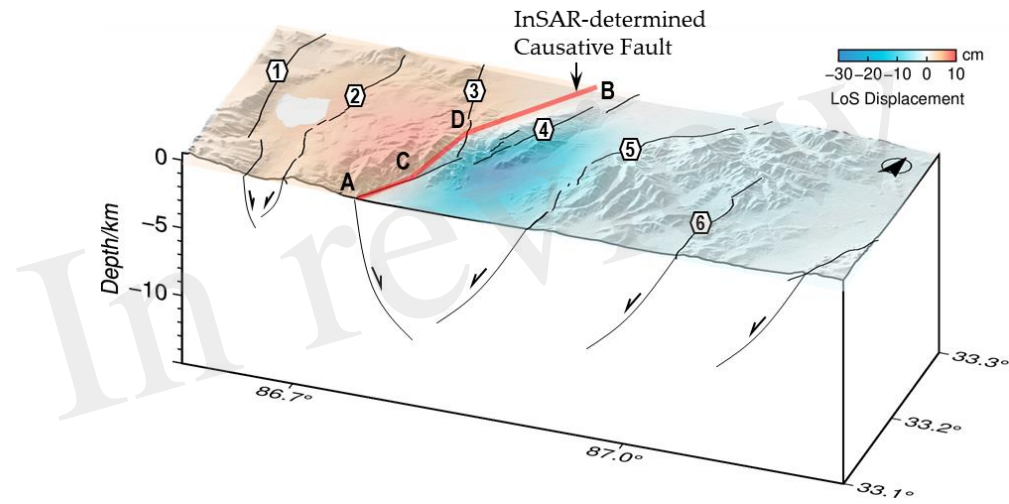


Figure 13. 3D structure of the active normal faults in the Yibu-Chaka graben and the causative fault of the 2020 Nima earthquake. Black lines in the section indicate normal faulting. Caption is as for Figure 2.

Table1. Fault plane parameters for the mainshock from InSAR studies, and as listed in the CENC, USGS, and GCMT Catalogs. The location indicates the centroid location or hypocenters, except for the InSAR models(*), which show the up-dip projection of the fault center to the surface. The geodetic fault geometry is inversed jointly with InSAR and GNSS datasets.

Model	Latitude (°)	Longitude (°)	Centroid (km)	Strike (°)	Dip (°)	Rake (°)	Slip (m)	Moment (10^{18} N.m)	non-DC (%)	Magnitude
CENC	33.19	86.81	10	10	50	-81				Ms6.6
USGS	33.144	86.864	10	20	61	-91		3.2	21	Mww6.3
GCMT	33.10	86.87	16.8	10	48	-88		5.01	43	Mw6.4
*Ji et al, 2021			7.3	28.4	48.3	-81.3	1.06	3.59		Mw6.3
*Yang et al, 2021			6.3	30	48.3	-80	1.2			Mw6.3
*Li et al, 2021	33.18	86.89	7.5	28	48	-87	1.5	4.7		Mw6.4
*Gao et al, 2022	33.18	86.88	6.9	28.8	49.4	-78.6	1.2	4.02		Mw6.28
*This paper	33.17	86.88	8.4	28	50	-79	1.16	6.4		Mw6.4